Chapter 6

Discussion

6.1 Magnetization reversal on transitions

In Section 5.1.2, it was mentioned that the Co/Ni double layer grown on the clean Cu(001) surface in an out-of-plane uniaxial anisotropy region spontaneously showed stripe domains as a result of minimizing the total energy, a sum of demagnetizing and domain wall energy. In Section 5.1.3, a jump-like magnetic domain wall motion and domain nucleation were reported upon increasing the substrate temperature up to above T_C, for a film with pure out-of-plane anisotropy. By elevating the temperature, the period of stripe domains got smaller, and just before the films turn into the PM phase, some domains were nucleated and stripe domains were split.

Upon increasing the film temperature, but in a low temperature range ($T < T_C$), thermal fluctuations are not so large and the change of spin direction is gradual. As a consequence, the demagnetizing energy may not be reduced so much, but the crystal structure maybe distorted, leading to a lower anisotropy energy [75]. As mentioned in Section 5.1.2, the wall energy is a sum of the exchange energy and the anisotropy energy. So lowering the anisotropy energy leads to the reduction of domain size, in other words, it increases the total wall length per unit area. The reduction of the stripe domain size is seen in Fig. 5.5. Because of a small gradient of the Ni film thickness, T_C slightly varies as well laterally. In the images, the decrease of the stripe domain width with the normalized temperature T/T_C is seen.

Just before reaching T_C, it was observed that the stripe domains transformed into the bubble-shaped domains, and also domains were nucleated, as suggested by Garel and Doniach [76]. This is a transition of breaking of symmetry due to the fluctuation of spins. The walls do not have preferable direction, showing round-shaped domains. In this unstable state, a lateral motion of domains by spin fluctuation was also observed. Finally, the FM layer transits to the PM state.

6.2 Motion of the spin reorientation transition line

In Section 5.1.2, it was reported that the epitaxially grown Co/Ni double layer on the clean Cu(001) surface in which the Co layer was grown as a wedge shows stripe domains in an out-of-plane uniaxial anisotropy region close to the SRT . The shrinking of stripe domain width as approaching the SRT was discussed in terms of a competition of magnetic energy terms. The saturation magnetization was assumed to be constant because the variation of the Co thickness is small in the field of view of only 50 μm diameter, and the anisotropy energy was assumed to change linearly with Co thickness.

Jump-like magnetic domain wall motion was observed when depositing more Co material. The field of view was first set to the top-left of the SRT line, where the Co layer is thinner, and the double layer has out-of-plane easy axis of magnetization. By deposition of Co, the SRT line was pushed into the field of view moving towards top-left, and to the thinner Co region along the slope of the Co wedge. The motion of the SRT is governed by discontinuous wall jumps introduced in Fig. 5.6, that lead to a shrinking width of the stripe domains. This can be explained by thermally activated domain wall motion, as introduced in Section 3.1. In Fig. 6.1, the creeping of stripe domains in the wedge-shaped Co layer is shown by a cartoon. The area in the left hand side has a perpendicular anisotropy (no Co and thinner Co region, light grey in color), and the film has an in-plane anisotropy on the right hand side (thicker Co region, dark grey). In between, stripe domains are formed with up and down perpendicular magnetization (Fig. 6.1 (a)). The magnetization directions are indicated by arrows. A line is on the border between stripe-domain and single domain regions at the critical thickness of Co, d_{Crit}. By depositing more Co, the position of d_{Crit} shifts to the left hand side (Fig. 6.1 (b)), but the domain structure stays the same. The wall motion is prevented by the energy barriers created by surface defects and crystal roughness. As depositing more Co (c), the out-of-plane anisotropy energy is more reduced, then the wall energy becomes smaller, therefore the imbalance between the gain in demagnetizing energy and the cost in wall energy is greater than pinning barriers. This imbalance of demagnetizing energy can be regarded as a local effective field for increasing the length of smaller stripe domains towards the region with thinner Co thickness. Thus one of the domains makes a big jump to compensate the total magnetic energy.

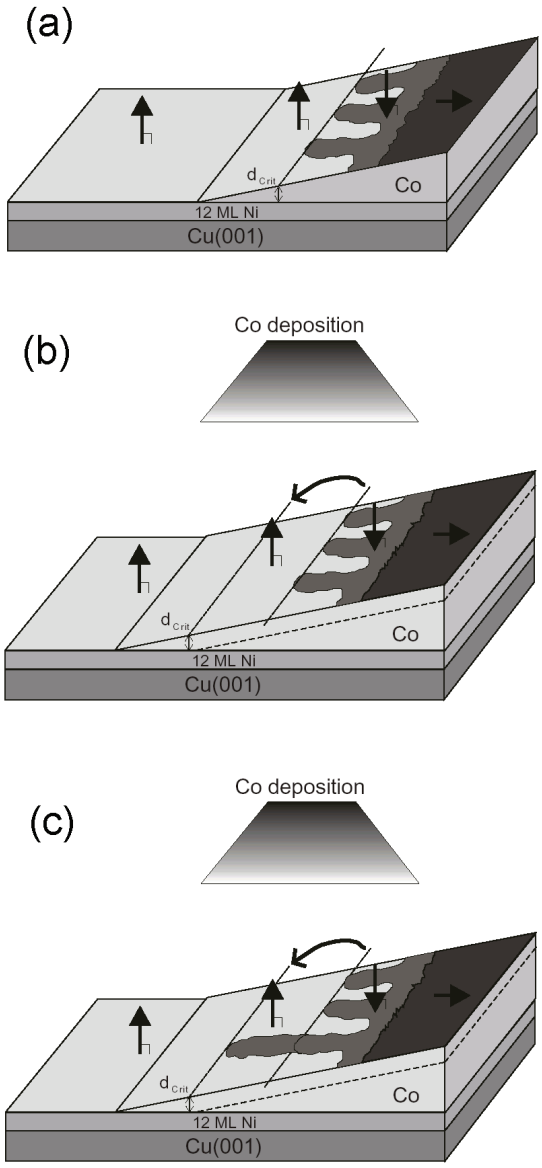

Figure 6.1: Cartoon of motion of the SRT line by wall jumps while depositing more Co material on the wedge Co film on Ni/Cu(001).

6.3 Influence of coupling energy on magnetization reversal

In Figs. 5.10 and 5.11 in Section 5.2, magnetization reversal of the FeNi layer of a spin-valve like trilayer is studied by a single-pulse experiment. It was shown there that the magnetization reversal of the FeNi layer for switching from parallel to anti-parallel (Configuration A) or from anti-parallel to parallel (Configuration B) to the Co magnetization direction is quite different. For Configuration A, a transition in the magnetization reversal mechanism was observed when $\mu_0 H_{pulse}$ was increased from 4.8 to 16.3 mT. For the higher amplitude of pulses the density of nucleation centers increases and the domain size decreases. For Configuration B, observations could be made only over a much narrower field range, and no significant difference in the density of nucleation centers could be deduced from the images.

The same effective field pulses ($H_{eff} = H_{pulse} - H_{coupl}$ for Configuration A and $H_{eff} = H_{pulse} + H_{coupl}$ for Configuration B) applied to the sample initially give rise to different magnetization reversal processes. In Fig. 5.11 (b) and (h) the same $\mu_0 H_{eff}$ (around 7.0 mT) is applied, but the domain configuration after application of one pulse is very different. While it is difficult to conclude about differences in nucleation densities in the two cases, it is clear that in Configuration B, where the FeNi layer is switched towards the Co magnetization direction, domain wall propagation is easier than in Configuration A. When the magnetization of the FeNi layer is switched against the Co magnetization direction (Configuration A), the magnetization reversal took place mainly by nucleation of domains.

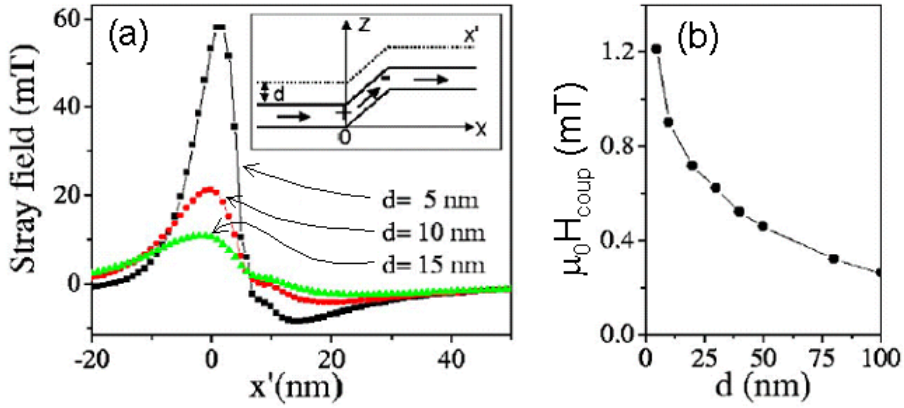

Figure 6.2: (a) x-component of the stray field emitted by a 5 nm thick Co film around a 6 nm wide topological step, calculated for a constant distance of 5 nm, 10 nm, and 15 nm from the Co surface. Inset: sketch of the profile of the Co layer and its magnetization (arrows) around a topological step perpendicular to the easy magnetization axis. The dashed line shows a constant distance from the surface. (b) Calculated coupling field between FeNi and Co layers for different spacer thicknesses. The line is a guide to the eye. These figures are from Ref. [46].

The magnetic coupling energy is shown to play an important role in these measurements. In Ref. [46] the locally generated stray field at the step-bunches from the 5 nm thick Co layers have been calculated for three different distances from the Co surface (by J. C. Toussaint), like shown in Fig. 6.2 (a). The maximum field can reach several tens of mT at 5 nm distance from the Co surface. Note that the coupling arising form this stray field is Orange peel type and favors parallel magnetization in the two FM layers. In Configuration B, this coupling field is thus in the direction to help the wall motion. In Configuration A, in contrast, it locally blocks the wall motion, leading to the increase in the number of nucleation cites and the observation of small domains. The values of the coupling field as a function of the spacer layer thickness are shown in Fig. 6.2 (b). For a 10 nm thick spacer layer, the calculated coupling field is about 0.8 mT, which is about a half of that derived from the Kerr effect experiment, but in the same order of magnitude.

Quasi-static Kerr effect measurements were performed to confirm that no wall motion occurs in static conditions, between pulses. One loop from the Co layer and different minor loops from the FeNi layer are shown in Fig. 6.3. These measurements could not be performed on the original piece of sample used in Section 5.2, since for the PEEM experiments the protecting layer had been

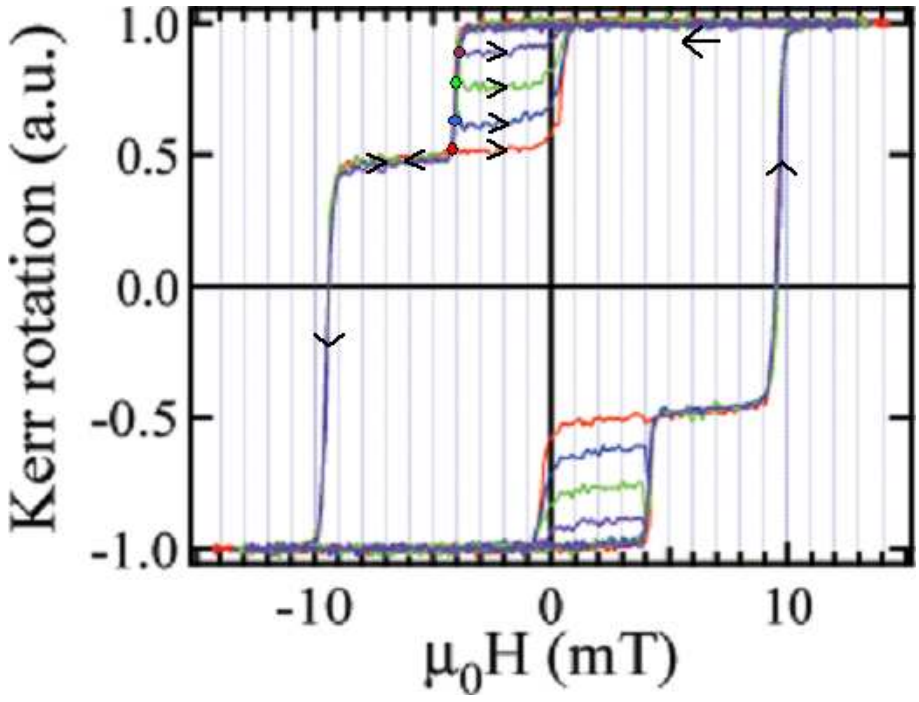

Figure 6.3: Hysteresis loops from a 5 nm $Fe_{20}Ni_{80}$/10 nm Cu/5 nm Co spin-valve-like trilayer system. Double-stepped loops indicate that the coercivity of FeNi (low) and Co (high) layers are different. Minor loops of the FeNi layer are shown for different reversal fields, indicated by small circles.

partially sputtered off. Instead of that, one of the pieces from the same waver with a film deposited in the same run, but at a different position was used. It is seen that the coercivity of the Co layer is not exactly the same as in Fig. 5.10, but the coercivity of the FeNi layer and the coupling field are almost the same.

Starting from the situation in which the FeNi and Co layers are saturated in the same direction (Configuration A), the external field was vamped into the opposite direction, and then reversed back before fully saturating the FeNi layer to the other direction. The (nearly) square-shaped loops show that the magnetization of the FeNi layer is almost constant until it is saturated back to the initial magnetization. This indicates that, at least under quasi-static conditions, after switching off the external magnetic field there is no domain wall motion induced by the coupling to the Co layer. It proves that the magnetization does not change when the field is decreased to zero on different points in Fig. 5.10 during the switching of the FeNi layer, i.e., that the switching process is irreversible.

In concluding, we can say, for a fast magnetization reversal, micromagnetic effects have to be taken into account. The magnetization reversal with a higher density of domain nucleation centers may not be preferable for a fast reversal. It will be discussed in Section 6.6 that the domain wall energy may slow down the speed of wall propagation when domains are small. The size of nucleated domains will be obtained from a simulations, and will be about 0.2 μm^2. It will be also discussed in Section 6.7 that the high density of nucleation centers leads to 360° domain walls, which are hard to be removed because of the domain wall interaction, leading to slow down the reversal. This can explain the tilted hysteresis loop of sample D (Fig. 5.18). However, when the magnetization reversal is being helped by the coupling field, fast magnetic domain wall propagation has been observed when two domains get connected (Section 6.7).

6.4 Mobility of wall motion

To estimate the domain wall velocity, v, as a function of field in the FeNi layer which magnetically couples to the Co layer (SV like trilayer), H_{coupl} has to be taken into account. From Fig. 5.12 in Section 5.2.3, v as a function of $\mu_0 H_{eff}$ is derived. When the magnetization of the FeNi layer reverses against the Co magnetization ((i) and (ii) in Fig. 5.12), $\mu_0 H_{coupl}$ (= 2.0 mT) is against the pulse field, therefore $H_{eff} = H_{pulse} - H_{coupl}$. This results in effective fields $\mu_0 H_{eff}$ = 3.0 mT and 4.1 mT for (i) and (ii), respectively. On the contrary, when the FeNi magnetization reverses to the Co magnetization ((iii) in Fig. 5.12), $H_{eff} = H_{pulse} + H_{coupl}$, and $\mu_0 H_{eff}$ is 5.3 mT, with $\mu_0 H_{pulse}$ = 3.3 mT. In this experiment, the domain wall motion obtained here was in the viscous regime or perhaps in the regime of wall motion above H_{Walker} (see Section 3.3), since the effective fields were well above the coercivity of the FeNi layer, and up to close to H_{Walker}, which is around 5 mT for FeNi derived from Eq. 3.26 taking α = 0.01. The value of $\mu_0 H_{Crit}$ is estimated to be about 2 mT. This value was obtained using Eq. (3) of Ref. [77] which relates E_p, the activation energy, to H_{Crit}. E_p should be equal to $V_B M_S H_{Crit}$ without external field, where V_B and M_S are the Barkhausen volume and the saturation magnetization of the FeNi layer, respectively. E_p and V_B were obtained from

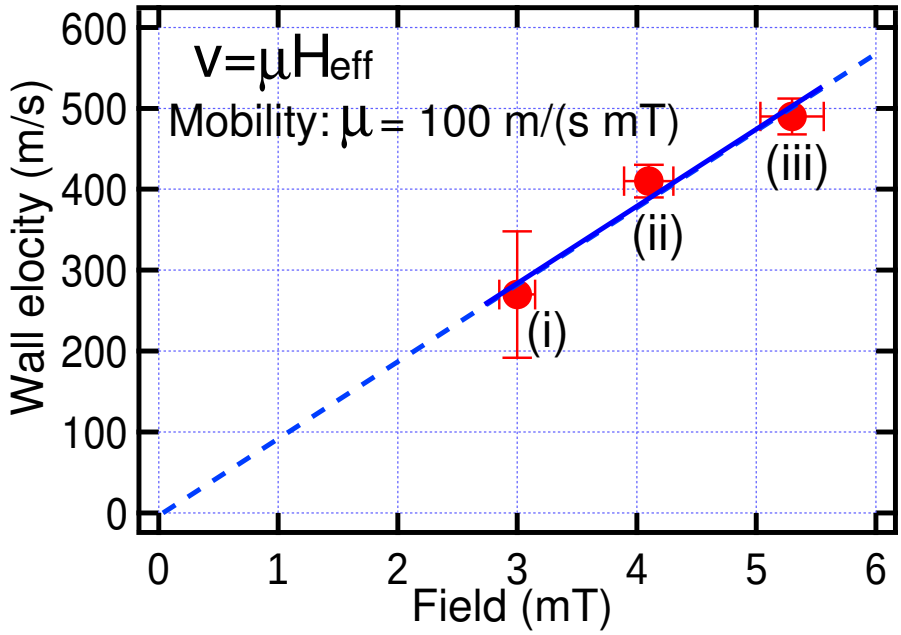

Figure 6.4: Domain wall speed as a function of effective field extracted from Fig. 5.12. The effective field was obtained by addition or subtraction of the pulse field and the coupling field (2.0 mT) for Configurations B and A, respectively. The mobility μ of the wall motion was obtained by a linear fit to v=μH_{eff}, which resulted in 100 m/(s mT).

H vs.dH/dt measurements [55], giving 2.98×10^{-19} J (1.86 eV) and 1.88×10^{-22} m^3, respectively. $\mu_0 M_S$ was taken as 1 T.

In the viscous regime, the speed of domain wall motion increases linearly with H_{eff}. Our data are well fitted using v = μH_{eff}, where μ is the domain wall mobility (details see Section 3.2). The obtained value of μ is 100 m/(s mT) $\pm$ 10 %. The domain wall mobility depends on the damping parameter α and the domain wall width of the permalloy layer, since $\mu = \gamma\Delta/\alpha$ (see Chapter 3 and [8]), where γ is the gyromagnetic ratio (= 1.79×10^{11} T^{-1}s^{-1}) and Δ is the domain wall width parameter. In the case of a Bloch wall, Δ equals the wall width [78]. For a layer thickness of 5 nm, the domain walls in the FeNi layer are supposed to be of the Néel type [39, 79, 80]. In the case of a Néel wall, the relation between the wall width and the domain wall width parameter Δ is not known, and an evaluation of the damping parameter α from the present measurements is therefore limited to a rough order-of-magnitude estimate. Setting the wall width parameter Δ equal to the exchange length of FeNi (about 5.5 nm) results in a value of 0.01 for α results. This is reasonable considering other experimental values, which range from 0.008 to 0.013 for FeNi film thicknesses between 10 and 50 nm [59, 81–84].

Previously, on the contrary, for 30 and 10 nm-thick FeNi layers, values of 380 m/(s mT) and 300 m/(s mT) have been reported, respectively [79, 80]. These data are for thicker films, but show a higher mobility. This contradiction may arise from the large roughness of our sample due to the steps with a height of about 6 nm. This roughness may lead to a domain wall mobility that is lower than in flat films.

6.5 Influence of anisotropy energy on the magnetization reversal

In Section 5.3 and 5.4, it was observed that the magnetization reversal properties in the ns range of two samples, one with uniaxial magnetic anisotropy energy (sample C) and one without (sample D), are quite different. The domain wall motion in sample D shows nearly 100% reproducibility. On the contrary, domain wall motion in sample C is not reproduced exactly in successive bipolar field pulses. Since both samples were deposited on the same substrate using the same technique, the quasi-static coercivity of the FeNi and the Co layers and the interlayer coupling strength are quite similar. I attribute these differences in their dynamic behavior to the difference in the magnetic anisotropy.

In sample C, the domain walls are parallel to the easy axis of magnetization to accumulate less magnetic charges than domain walls in other directions. In sample D, however, the direction of walls are irregular, and the size of domains is much smaller than in sample C (micron size). Since sample D has an almost negligible anisotropy energy in the film plane, the domain walls have no preferable direction.

A dependence of the reproducibility of the wall motion on the anisotropy energy was found by comparing these two samples. For sample C, the wall motions were not the same on each magnetic field pulse. This is seen from the fuzzy grey contrast on the pump-probe experiments (Fig. 5.15 (b)), and also in Fig. 5.16 one can clearly see that after application of magnetic pulse fields the domain structures are not the same. The wall velocity should be almost the same for each pulse, because the wall velocity depends only on the amplitude of the field pulses in the viscous regime (Eq. 3.23). However, by the field pulse the domain walls are moved over a large number of Barkhausen areas, so that the exact stopping position is always a bit different. In sample D, however, nearly 100% of reproducibility was observed. A high density of nucleation centers can be deduced from the *tilted* Kerr loop in Fig. 5.18, and also directly from XMCD-PEEM images in Fig. 5.19. This large density of nucleation centers may prevent the wall propagation. It was not possible to saturate the FeNi fully by ns-short magnetic field pulse even with higher amplitude, the used maximum field was around 10 mT. The 360° domain wall created by strong wall-to-wall interaction was hard to be removed. Because of this additional energy barrier to prevent the wall motion, the wall velocity was lowered and showed nearly the same motion on each field pulse.

6.6 Influence of domain wall energy on wall motion (1)

In Section 5.5.2, the nucleation and subsequent expansion of domains in the FeNi layer of the MTJ like trilayer system was reported using XMCD-PEEM experiments with the pump-probe technique. A linear dependence of the speed of perimeter extension, v_p, on the amplitude of the field pulses was observed. However, there was a delay time of domain expansion, which depended on the amplitude of the field pulses. This delay can be fully understood by taking into account the wall energy, γ_{DW}.

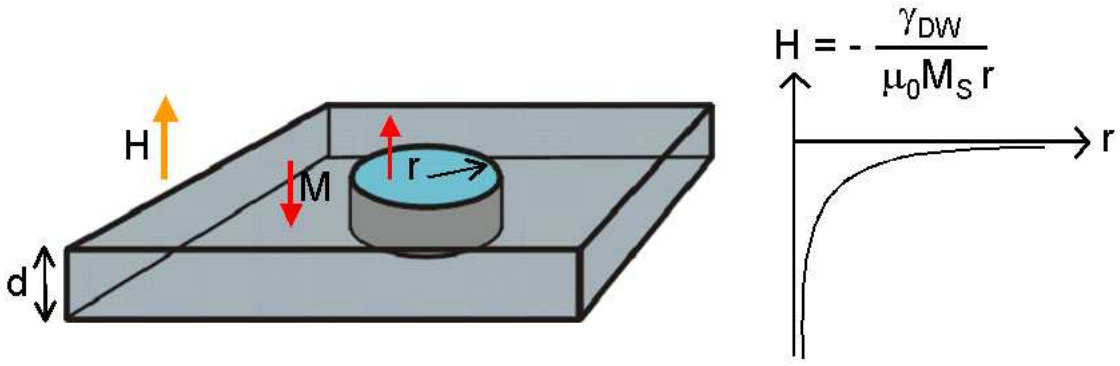

Figure 6.5: Influence of domain wall energy on domain expansion. The external field, H, nucleates a domain with radius, r, in a magnetic film with out-of-plane anisotropy. The domain will expand by the Zeeman energy, but the wall energy tries to keep it small. The negative field for the domain expansion is written on the right side, which is proportional to the inverse of the domain size.

To understand how the wall energy acts on the wall motion simply, let's assume that a magnetic film has an easy axis of magnetization perpendicular to the film plane (Fig. 6.5). By the external field, H, a domain will be nucleated, and it can be round-shaped with radius, r. The domain will expand to reduce the Zeeman energy ($E_Z = \mu_0 M_S H\, \pi r^2 d$), but the energy related to the domain wall energy, γ_{DW}, ($E_{wall} = \gamma_{DW} 2\pi r d$) will increase, where d is the film thickness, and M_S is the saturation magnetization ($\mu_0 M_S$ = 1 T for FeNi). The differences of E_Z and E_{wall} for a small change of r will be equal, then

$$\frac{dE_Z}{dr} = \frac{dE_{wall}}{dr}. \tag{6.1}$$

Then the external field balances the effect of the wall energy. We can thus define an effective field hindering the expansion of the domains due to the increase of wall energy, H_{wall}, as

$$H_{wall} = -\frac{\gamma_{DW}}{\mu_0 M_S\, r}. \tag{6.2}$$

H_{wall} is proportional to the inverse of r, schematically shown on the right hand side of Fig. 6.5.

In reality for the sample E, the FM layers have an in-plane anisotropy and the nucleated domains were elongated along the easy axis with an aspect ratio around 4:1 (see Fig. 5.23 and 5.24). Thus H_{wall} as a function of perimeter, P, derived from Eq. 6.2 will be

$$H_{wall} = -\frac{\gamma_{DW}}{\mu_0 M_S}\frac{1}{0.16\,P}. \tag{6.3}$$

The factor 0.16 appeared by converting r to P, in which the circumference with r and the perimeter were kept the same, and the aspect ratio of the ellipse-shaped domains, 4 to 1, was taken into account.

The total effective field containing the pulse field, the coupling field, and the field due to the wall energy can be written

$$H_{eff} = H_{pulse} - H_{coup} - \frac{\gamma_{DW}}{\mu_0 M_S}\frac{1}{0.16\,P(t)}. \tag{6.4}$$

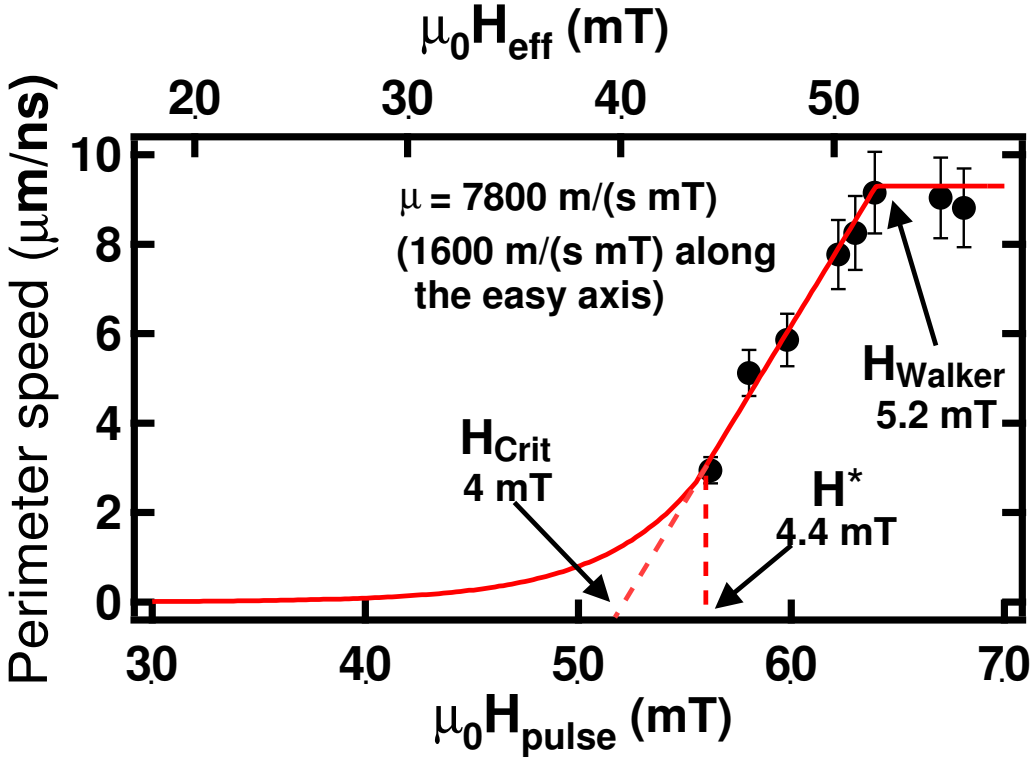

Figure 6.6: Perimeter speed vs. $\mu_0 H_{pulse}$ (on bottom axis) and $\mu_0 H_{eff}$ for $P \to \infty$ (on top axis). The linear-fit to six of the data points (black broken line) indicates that up to 5.2 mT of $\mu_0 H_{eff}$ the extension of the perimeter (the wall motion) is in the viscous regime. The exponential part at lower field regime ($\mu_0 H_{eff} < 4.4$ mT) is drawn using the upper formula of Eq. 6.6. In the higher field region, above H_{Walker}, the perimeter speed is assumed to be constant (9.3 μm/ns).

The second and the third terms on the right hand side represent the negative fields, hindering or slowing down domain expansion. Since the perimeter speed, dP(t)/dt, is a function of H_{eff}, given by Eq. 6.4, this represents an inhomogeneous non-linear differential equation. In the following, I will try to simulate the experimental data by numerically evaluating P(t).

For the FeNi layer with 4 nm-thickness, domain walls are of the Néel type [39]. In this case, the domain wall energy can be approximated by $\gamma_{DW} = \sqrt{AM_S^2/(2\mu_0)}$. Using A = 1.3 $\times$ 10^{-11} J/m for the exchange constant of FeNi, one obtains γ_{DW} = 2.3 mJ/m^2. In this study, however, an effective domain wall energy, γ_{eff}, with a smaller value, 0.4 mJ/m^2, had to be used for the simulation in order to describe the experimental data. This smaller value may arise from the fact that a repulsive interaction between the walls of an ellipse, which is not included in Eq. 6.2, would lead to a lower γ_{eff}. And also, just after the nucleation of the domains their shape could be more rounded. For the same total wall energy, a smaller γ_{eff} needs to be used in that case.

In Fig. 6.6, the speed of perimeter expansion, v$_P$, (the slope of linear fits to the experimental data of Fig. 5.25) vs. $\mu_0 H_{pulse}$ and $\mu_0 H_{eff}$ (for the case of infinitely large P) is plotted. In the range from 5.5 mT to 6.4 mT of $\mu_0 H_{pulse}$, a linear fit could be applied, namely, the wall motion was in the viscous regime. The mobility of *perimeter extension*, μ, of 7800 m/(s mT) $\pm$10 % was obtained from the slope. The mobility of *wall motion* in the direction of the easy axis of magnetization is then 1600 m/(s mT) $\pm$10 %, taking into account the aspect ratio of the ellipse-shaped domains (4:1). The two data points with the highest amplitudes of the field pulses (6.70 mT and 6.81 mT) are not included in the linear-fit, they seem to be above H_{Walker} (see Section 3.3).

In Fig. 6.7, the domain expansion with 2 ns for three different amplitudes of the field pulses is compared. Those 6 domain images of the FeNi layer were part of the data set that was used to plot Fig. 5.25. In the left column, 3 images which exhibit similar size of white domains were chosen but there were some differences after 2 ns (right column). From (a) to (b), the evolution of white domains is less than that from (c) to (d), due to the smaller amplitude of the field pulse. However, the change from (e) to (f) is not much different or even a bit less compared to the one from (c) to (d), even though the amplitude of the field pulse is higher. This confirms that saturation of v$_P$ is observed above about 5.2 mT of $\mu_0 H_{eff}$ (= $\mu_0 H_{Walker}$). Above H_{Walker}, v$_P$ is assumed to be constant, 9.3 μm/ns.

In the lower $\mu_0 H_{eff}$ regime in Fig. 6.6, before the wall motion comes into the viscous regime, thermally activated wall motion has to be assumed. In general, the extrapolation of the linear part of the viscous regime to the field axis leads to the critical field, $\mu_0 H_{Crit}$, which is at around a transition field from the thermally activated wall motion to the viscous wall motion. However, $\mu_0 H^*$ (= 4.4 mT) is taken as the transition field to draw the smooth curve in Fig. 6.6. To estimate v$_p$ in this region for use in the simulation, the following equation for the wall velocity can be used, shown in

Refs. [8, 11], and also in Section 3.1,

$$v = v_0 \exp(\frac{\mu_0 M_S H V_B - E_p}{k_B T}), \tag{6.5}$$

where V_B and E_p are the Barkhausen volume and the barrier energy, respectively. In the case of thin films, the Barkhausen length, L_B, will be $\sqrt{V_B/d}$, which is related to the displaced distance of a wall position by one wall jump. Then v_0 will be L_B divided by a time constant (10^{-9} s is used here). However, here, v_0 is related to the speed of perimeter extension, not simply the domain wall propagation, and the aspect ratio of ellipse-shaped domains has to be taken into account. By putting proper values for V_B, and E_p, 1.1×10^{-23} m^3 and 6×10^{-20} J (4.5 mT), respectively, a v_0 of 2.6 μm/ns is found.

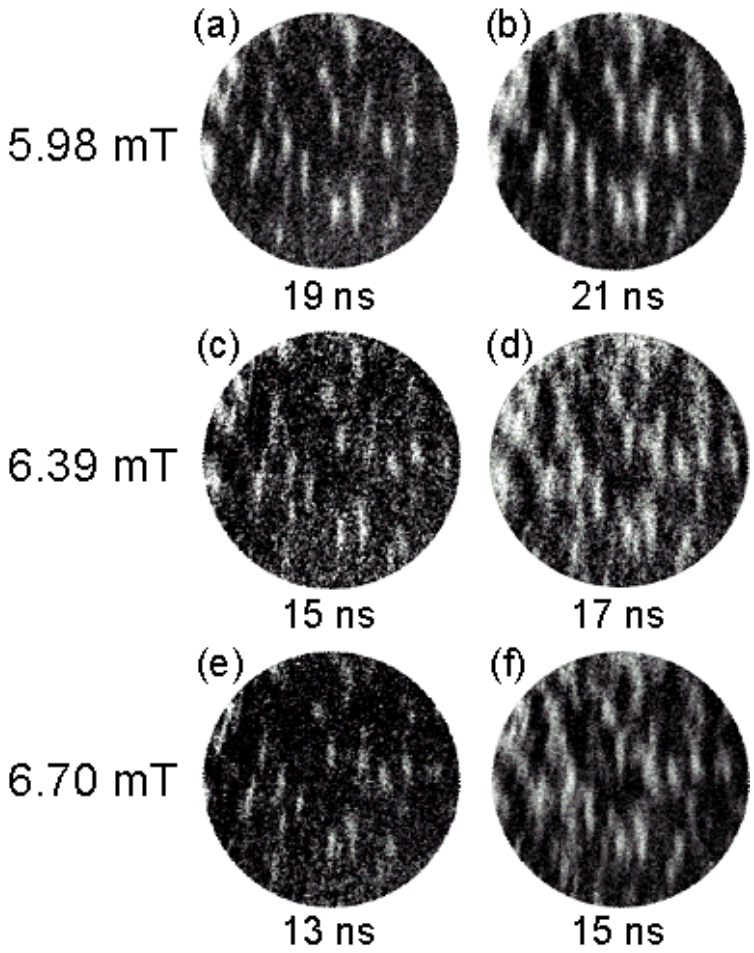

Figure 6.7: The expansion of domains in 2 ns are compared for three different amplitudes of $\mu_0 H_{pulse}$. Magnetic domain structures in the FeNi layer are shown. On the left column, similar domain structures were chosen, but domain sizes are different in the right column.

The solid curve in Fig. 6.6 showing the relation between v_P and the field ($\mu_0 H_{eff}$) is thus drawn by considering the three cases above,

$$v = \dot{P} = \begin{cases} v_0 \exp(\frac{\mu_0 M_S H_{eff} V_B - E_p}{k_B T}) & H_{eff} \leq H^* \\ \mu H_{eff} & H^* \leq H_{eff} \leq H_{Walker} \\ 9.3 \quad \mu m/ns & H_{Walker} \leq H_{eff}. \end{cases} \tag{6.6}$$

$\mu_0 H_{Walker}$ was read from Fig. 6.6 being around 5.2 mT, as $\mu_0 H_{eff}$ (top axis). H_{Walker} is expressed with $1/2\alpha M_S$ [20]. The damping constant, α, is often used as 0.01 for FeNi [16, 83, 84]. With this value one obtains $\mu_0 H_{Walker}$ as 5 mT, which is in good agreement with the experimentally obtained value.

The perimeter extension after the nucleation up to $\mu_0 H_{Walker}$ was numerically simulated by putting Eq. 6.4 into Eq. 6.6, where P is a function of time. The evolution of P was calculated with 1 picosecond time increment and plotted in Fig. 6.8 by solid curves for all amplitudes of the field pulses. The initial perimeter, P(t = 0), was set to 2.4 μm. If it is so, the width of nucleated domains

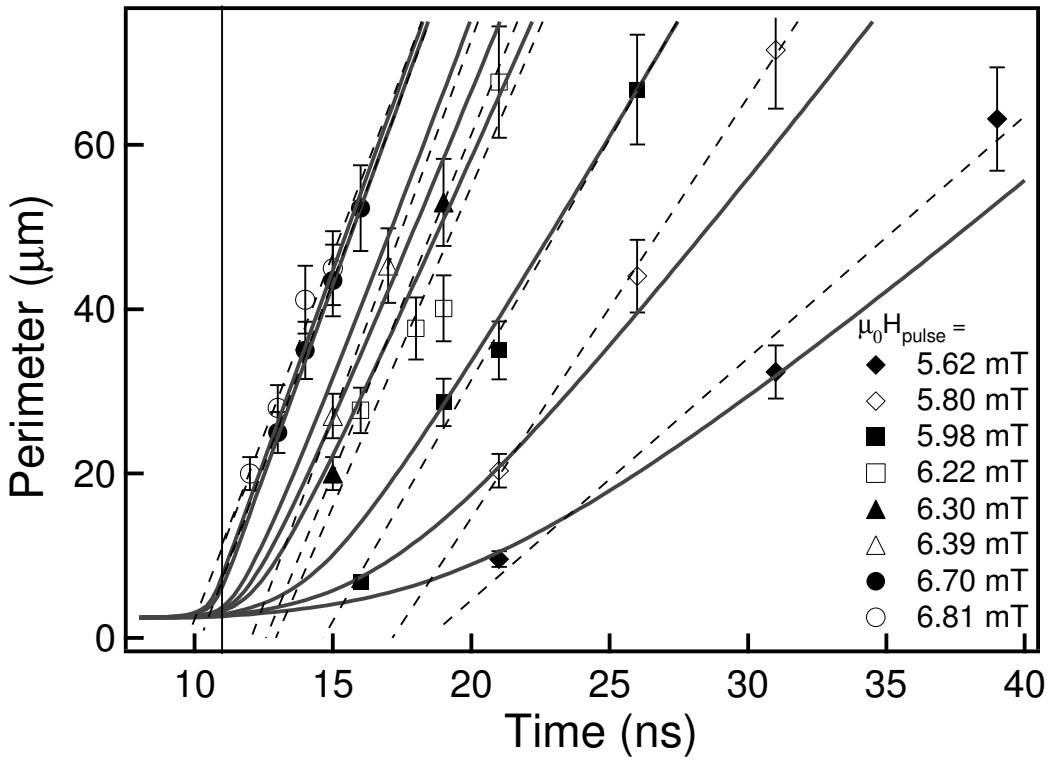

Figure 6.8: The same experimental data as in Fig. 5.25, extension of the perimeter vs. time on the plateau of the second positive pulse for several amplitudes of the field pulses. Black broken lines are linear fits to the data. In addition, the wall extension was simulated and shown as solid curves.

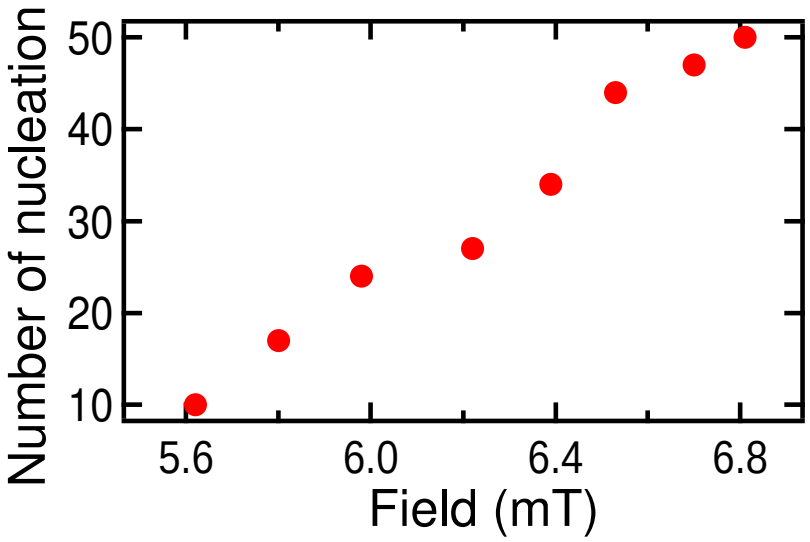

Figure 6.9: Number of nucleation centers in the field of view as a function of amplitude of the field pulses. The number of nucleated domains increases with field amplitude.

will be around 0.24 μm, which is too small to detect by the PEEM with the lateral resolution of $\sim$1 μm. The pulse shape was simplified such that the field increases linearly with time during the rise-time, the slope thus being $\mu_0 H_{pulse}/11$ (mT/ns). After 11 ns, the field is constant up to the end of the plateau. The simulation fits quite well to the experimental data (Fig. 6.8). It shows that the perimeter extends slowly with time when it is small, and after some time, depending on H_{pulse}, v_P shifts into constant speed. It is seen that for higher $\mu_0 H_{pulse}$ (6.70 mT and 6.81 mT), P started to expand on the rise-time of the H_{pulse} before 11 ns, this was also seen in the experiment (see Appendix).

In the above simulation it was assumed that there is no delay in the domain nucleation. Then the apparent delay of domain expansion (linear fits in Fig. 5.25) was explained by an initially lower speed of domain expansion caused by the domain wall energy. To confirm it, the number of nucleated domains in the field of view was counted, and plotted as a function of amplitude of the field pulses in Fig. 6.9. It is clear from the magnetic domain images in the Appendix that the number of nucleated domains increases with field, and it can be assumed that each nucleation center has different nucleation field. It was also observed all the domains were nucleated at the beginning of the field pulse, and no nucleation was observed later on, i.e., the number of domains did not increase during the field pulses. This indicates that the domains were immediately nucleated when the pulse field reached the nucleation field.

6.7 Influence of domain wall energy on wall motion (2)

In the case that two domains are close together, the wall energy tends to make them merge, leading to a faster domain wall motion (Section 5.4). Here, again the domain wall energy plays an important role for the wall propagation, and the Zeeman energy caused by H_{pulse} and H_{coup} has to be taken into account.

Expansion of domains along the magnetization axis, perpendicular to the magnetization axis, and the merging of two domains are schematically explained in Fig. 6.10. In Fig. 6.10 (a), the expansion of a rectangular domain of width w and length L along the magnetization axis by δL towards the top and bottom of the image, as indicated by the small thick lines, is shown. The effective energy acting on domain expansion can be written as (dimension: Joule)

$$E_{eff} = -2\mu_0 M_S (H_{pulse} - H_{coup}) \delta L w d + 4\gamma_{DW} \delta L d, \tag{6.7}$$

where the first and second terms on the right hand side are the Zeeman and the wall energy, respectively. For the film thickness d considered here (5 nm), domain walls are of the Néel type. In this case, the domain wall energy can be approximated by $\gamma_{DW} = \sqrt{A M_S^2/(2\mu_0)}$. Using A = 1.3×10^{-11} J/m for the exchange constant of FeNi, and $\mu_0 M_S$ = 1.0 T, one obtains γ_{DW} = 2.3 mJ/m^2.

If w = 1.5 μm, E_{eff} is about zero, leading no domain wall propagation. In the case, w is smaller than 1.5 μm, E_{eff} is positive. These behaviors are seen in Fig. 5.20 (c). In the regions where domains do not get connected, a displacement of walls is very a little indicated by thin grey area. However, in the regions where two or three small domains are close together, fast domain wall motion is observed, which will be discussed later.

Fig. 6.10 (b) shows the case when the same domain is expanded along its width. In this case, the head-on charged domain walls at the top and bottom have to get longer. Because of the additional magnetostatic interaction between the domains, these walls have a higher specific energy $\gamma^{\star}_{DW} > \gamma_{DW}$. This leads to $\delta w < \delta L$. It was seen in Fig. 5.20 that the domains were expanded mainly in a vertical direction in the images.

The energy penalty $\Delta\gamma_{DW}$ may be significantly reduced or may even reverse sign if two existing domains merge together. Such a case is schematically depicted in Fig. 6.10 (c), where the pointed ends of two domains merge upon application of an external field. In this case, the (partly charged) domain walls indicated by thick dotted tilted lines disappear and are replaced by (uncharged) vertical domain wall sections plotted by thick continuous lines. $\Delta\gamma_{DW}$ is now the difference in energy between the dotted and continuous wall sections, and may be zero or even negative, depending on the actual geometry. In the sample discussed here, the influence of $\Delta\gamma_{DW}$ on the wall propagation, and therefore on the speed of magnetization reversal, is significant and favors domain connections, as can be clearly seen in Fig. 5.20.

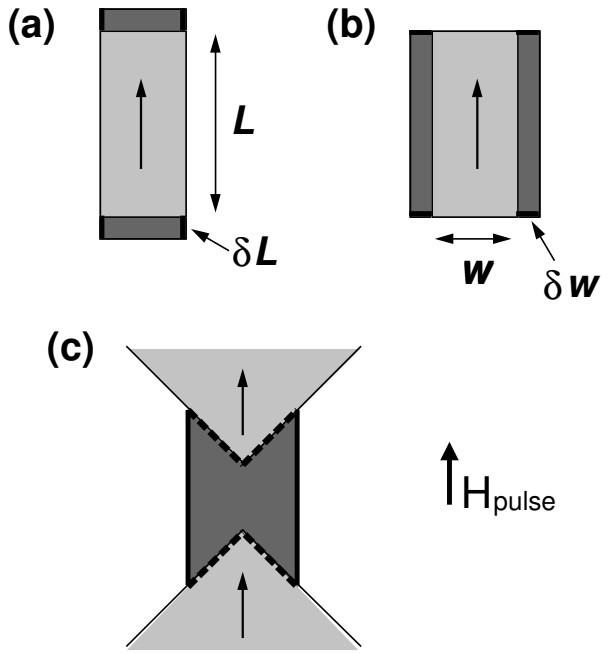

Figure 6.10: Schematic explanation for the increase or change in domain wall length upon magnetization reversal. (a) Expansion of a rectangular domain of length L and width w along the magnetization axis, (b) expansion of the same domain along its width, and (c) merging of two domains. The increase of the domain area by the darker area is accompanied by the creation of domain wall sections depicted by fat solid lines. While in cases (a) and (b), the total domain wall length is increasing, in case (c) the domain wall sections shown by dotted lines disappear, leading to a more favorable domain wall energy balance and higher domain wall speed.

In general, $\Delta\gamma_{DW}$ scales inversely with the size of the domains, such that it becomes more important when the magnetization reversal proceeds by nucleation and expansion of many small domains. It has been shown that for fast magnetization reversal, an increase in dH_{ext}/dt is accompanied by an increase in the number of nucleated and subsequently expanded reversed domains. This behavior is observed well in Fig. 5.11 in Section 5.22, in which when the magnetization of the FeNi reversed from parallel to anti-parallel to the magnetization in the Co layer (Configuration A), the number of nucleation centers increased and size of domains were smaller with higher amplitude of the field pulses. So the influence of the domain wall energy will consequently play a role exactly in cases in which high reversal speeds, and hence become important for the fast magnetization reversal of spin valve devices.

6.8 Stray field influence on the domain nucleation

In the time-resolved XMCD-PEEM experiments with sample E (Section 5.5.2), line-shaped domains are nucleated in the FeNi layer at the position where the domain walls exists in the Co layer. The effect of stray fields of domain walls in one layer on the magnetization of the other layer in FM/non FM/FM trilayers in static conditions has been treated quantitatively by several authors [53, 85–87].

In order to get a more precise idea of the influence of stray fields emitted by domain walls, a micromagnetic simulation using a code based on a combination of the finite element method (FEM)

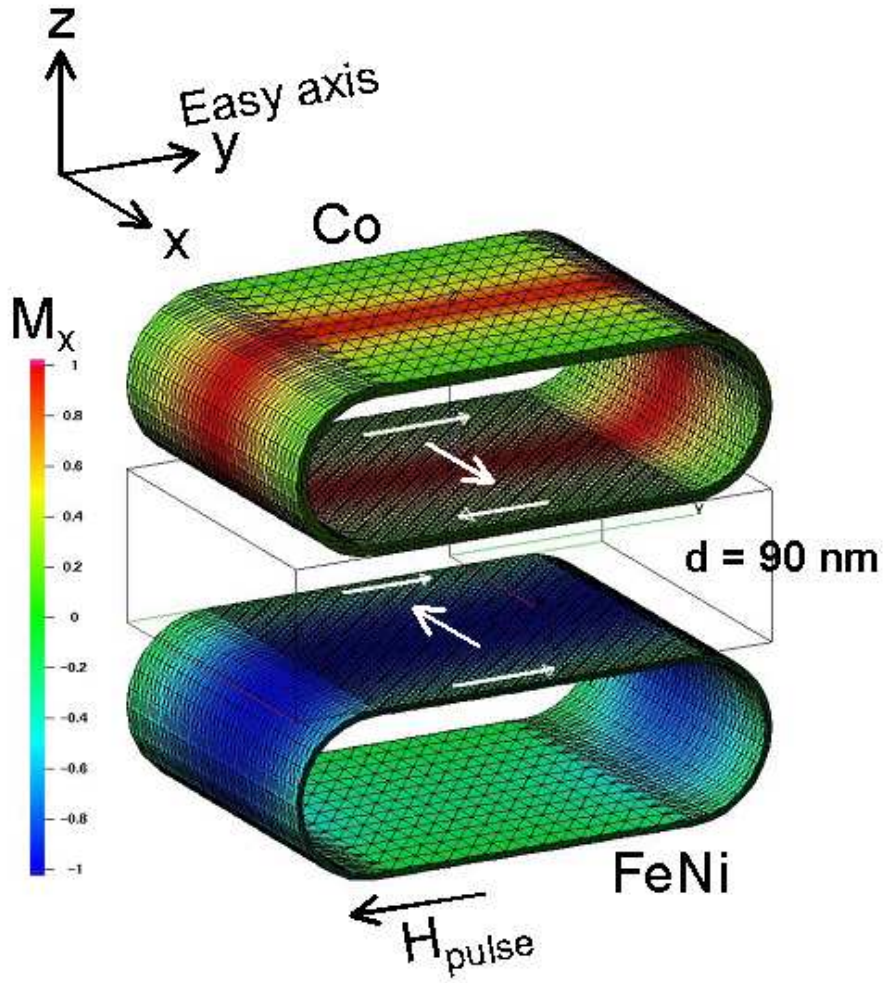

Figure 6.11: Simulation of a domain wall in the Co layer and its influence on the FeNi magnetization, for a spacer layer thickness of 90 nm. The ring shape is just to avoid the demagnetizing energy at the edge of the films. The color indicates the magnetization component in x direction. More details are in the text.

and the boundary element method (BEM) has been performed by Riccard Hertel. This FEM/BEM scheme is particularly suited to simulate magnetostatic interactions of FM particles, as described in Ref. [88]. The magnetic configurations are obtained by energy minimization. The exchange constant A and the saturation magnetization $\mu_0 M_S$ were taken as 1.3×10^{-11} J/m and 1 T for FeNi, while the values for Co were 3×10^{-11} J/m and 1.7 T, respectively. Experimentally determined values of 1720 J/m^2 (FeNi) and 11.2 kJ/m^2 (Co) were used for the uniaxial anisotropy constant. In Fig. 6.11, the FeNi layer (bottom) and the Co layer are shown. The ring shape of the film was chosen to avoid the demagnetizing effect at the edge of the films. The result of the simulation for a 90 nm thick spacer layer is shown. A Néel type domain wall was introduced in the center of the Co layer, between two domains with opposite magnetization directions along the easy axis.

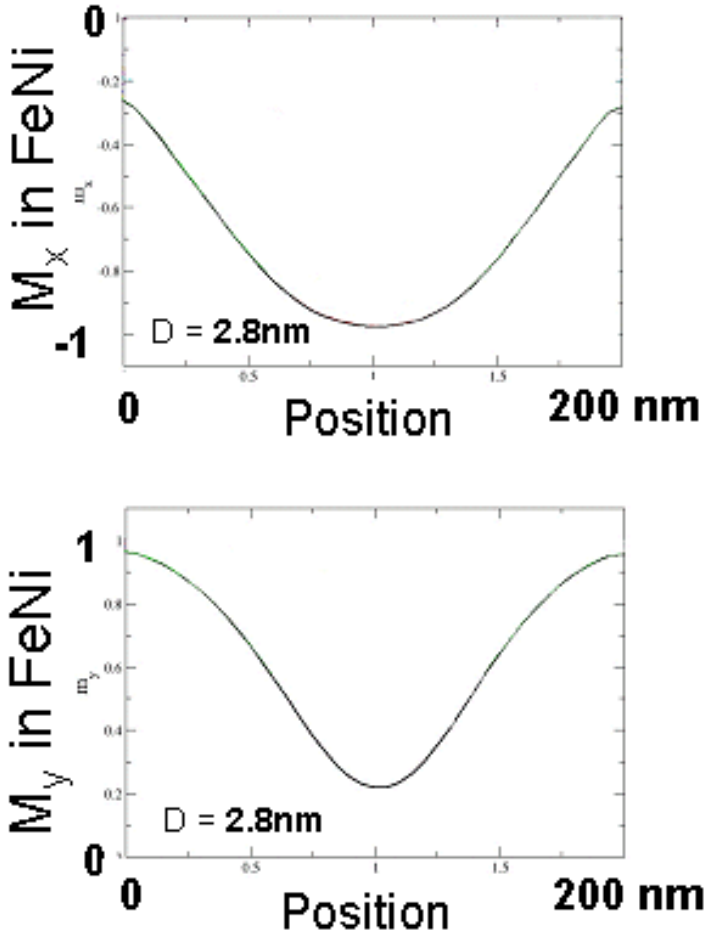

Figure 6.12: X and y components of the FeNi magnetization along the x axis for a spacer layer thickness of 2.8 nm, the same as in the sample used in the experiment.

The FeNi layer in the simulations was initially homogeneously magnetized along the y axis, and then its magnetization was relaxed together with the one of the Co layer to reach equilibrium. The final local magnetization components along the x axis are indicated with colors. The red, green and blue colors indicate magnetization along the positive x-direction, perpendicular to the x-axis, and along the negative x-direction, respectively. It is seen that the middle of the FeNi layer above the wall in the Co layer shows blue color. It means that the magnetization in the FeNi layer is strongly tilted in the direction perpendicular to the easy magnetization direction, opposite to the magnetization direction in the center of the Co wall. The profile of the x-component of the FeNi magnetization for 2.8 nm spacer layer thickness between the two FM layers is shown in Fig. 6.12 (a), while the y-component is given in Fig. 6.12 (b). The scale of the horizontal axes (200 nm) corresponds to the width of the films in the simulation of Fig. 6.11. It is seen that at the middle of the FeNi film the x-component is nearly –1, and the y-component is around 0.2, which indicates that the magnetization is almost perpendicular to the easy axis of magnetization. For magnetic field pulses applied along the easy magnetization axis, the torque on the FeNi moments is very small when these are aligned anti-parallel to the applied field. Above the Co domains, the FeNi moments are tilted away from this axis, and the torque acting on them is thus larger. The Co domain wall stray field acts like a transverse bias field that locally decreases the energy barrier for nucleation, significantly increasing the switching speed. The same principle has been exploited to obtain ultrafast magnetization switching in small magnetic structures, using an external transverse bias field [60]. The lowering of the nucleation field may increase the speed of the magnetization reversal in the storage devices.